GEOPHYSICS, VOL. 75, NO. 6 (NOVEMBER-DECEMBER 2010); P. W1–W12, 12 FIGS.
10.1190/1.3493638

Deconvolution imaging conditions and cross-talk suppression

Travis L. Poole[1], Andrew Curtis[1], Johan O. A. Robertsson[2], and Dirk-Jan van Manen[3]

ABSTRACT

Deconvolution imaging conditions offer improved resolution over standard, crosscorrelation-based imaging conditions. Additionally, these imaging conditions produce a result more directly related to a reflection coefficient than do crosscorrelation-based imaging conditions. In simple analytical cases, deconvolution imaging conditions also offer the possibility of eliminating crosstalk (i.e., energy in the image due to reflected energy arriving at a location at the same time as incident energy that did not cause the reflected energy) when the full up- and down-going wavefields are used. This means that in such cases, surface-related multiples can be eliminated from the image, or that multiple shots could potentially be fired simultaneously without degrading the image. However, this cross-talk-suppression property is not observed in most situations. We show that this is due to a number of issues: the correct order of deconvolution must be used, stabilization causes imperfect deconvolution, finite apertures lead to some of the signal being lost, and an assumption of horizontal stratification is often not being met. Further, imperfect knowledge of the incident and reflected field due to such factors as anisotropy, poorly estimated velocity fields, and measurement noise can also lead to imperfect deconvolution. Thus, deconvolution imaging conditions should not be counted on to completely eliminate crosstalk from images.

INTRODUCTION

The purpose of seismic imaging is to locate reflectors in the subsurface so that geology can be inferred. Thus, the desirable qualities of an imaging condition would include: being able to accurately locate interfaces that are present, imaging no apparent interfaces where there are none, and ideally providing further information about the physical properties of the rock near the interfaces. Deconvolution imaging conditions (see Claerbout, 1971; Valenciano and Biondi, 2003, and Schleicher et al., 2008) offer improvements in all of these areas over standard crosscorrelation, imaging conditions (Claerbout, 1971). They allow interfaces to be better located because of the improved resolution they offer. They have some ability to reduce crosstalk in the images thus reducing the risk of interfaces being identified where they do not really exist. Finally, the magnitude of the reflectors in a deconvolution image are more closely related to the reflection coefficient, making tractable some basic inferences about rock properties on either side of the interface. However, although these properties of deconvolution imaging conditions can be derived for simple analytical cases and are used to justify the use of such imaging conditions, they are not obtained in realistic cases. In this paper, we explain why this is so, and in particular we show that the cross-talk eliminating property is only achieved in the case of a horizontally stratified medium, and that even in such cases numerical issues such as stabilizing approximations and finite ranges of the variables can preclude the full advantages seen in the analytical case. However, the improved resolution is retained in practice, and the magnitude in the resulting images is more closely related to a reflection coefficient than those produced by crosscorrelation imaging.

The next section reviews the basic concepts of propagating the incident and received fields and using them to create an image. We then present deconvolution imaging conditions and provide a set of examples illustrating key points. After this we discuss the factors that lead to multiples not being properly removed from deconvolution images. The final section summarizes our conclusions.

WAVE PROPAGATION AND IMAGING

In seismic imaging, the source field is usually propagated computationally forward in time, into the subsurface. The reflected field is propagated backward in time. The two fields are then combined at each potential subsurface reflector or diffractor location, by using an imaging condition. The deconvolution imaging condition, like the crosscorrelation imaging condition, is based on the imaging concept introduced by Claerbout (1971): at a reflector, the reflected (usually up-going) energy will simply be a scaled version of the incident (usually down-going) energy. The scaling factor will be the reflec-

Manuscript received by the Editor 24 September 2009; revised manuscript received 11 May 2010; published online 20 October 2010.
[1]University of Edinburgh, Edinburgh, U. K. E-mail: travis.poole@ed.ac.uk; Andrew.Curtis@ed.ac.uk.
[2]Schlumberger Cambridge Research, Cambridge, U. K. E-mail: JRobertsson@slb.com.
[3]WesternGeco London Technology Centre, Gatwick, U. K. E-mail: DManen@gatwick.westerngeco.slb.com.

tion coefficient of the reflector. Or, stated another way, the time between the arrival of the incident field and the reflected field will decrease as the distance from the interface decreases; at the reflector the two fields arrive simultaneously. Thus, if we deconvolve the reflected field from the incident field at a reflector, the result will have energy at zero-time lag. At a location away from a reflector, there will be a time delay between the arrival of the incident energy and any energy reflected from elsewhere. Deconvolving the two fields at such a location should not produce significant energy at zero time lag. This is easy to see in the case of a single incident pulse, and a single reflected pulse, as shown in Figure 1. In the figure we see that when the incident and reflected pulses arrive at the same time, there is energy in the zero-lag of the deconvolution. However, when the pulses arrive at different times, the energy in the deconvolution occurs at a lag corresponding to the difference in arrival times. The deconvolution becomes more complicated when there are many reflections, and when the incident field is more complicated than a single pulse, because the two fields are not merely time-shifted-and-scaled versions of one another. Thus, there will be multiple time-lags with non-zero energy in the deconvolution of the two fields. However, the principle remains the same: when the reflected field contains a scaled copy of the incident field, arriving at the same time as the incident field, there will be energy in the zero-lag of the deconvolution. This

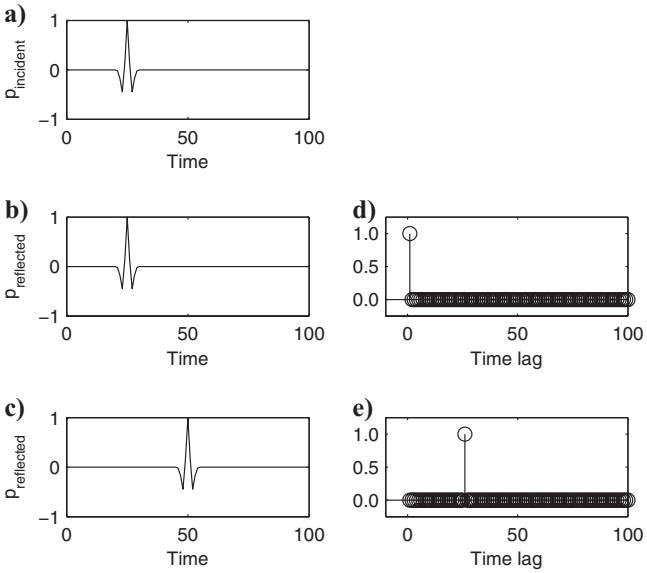

Figure 1. A simple example of deconvolution. The top frame (a) represents an incident pulse arriving at an image point in the subsurface. The two frames below (b,c) represent two possible reflected wavefields. The frames to the right (d,e) show the result of deconvolving incident field from the reflected fields to their left. The middle frames (b,d) represent what would be seen at the reflector's position. The incident and reflected pulses arrive at the same time, and the deconvolution of the two fields (d) has all its energy at zero time-lag. The bottom frames (c,e) represent what would be observed at a point away from a reflector. The incident field arrives first, then continues on to the reflector, generating a reflected pulse which propagates in the opposite direction and arrives at the image point some time later. The deconvolution (e) result has energy at the time-lag corresponding to the difference in arrival times of the two pulses. Note that in both cases, a discrete delta function is the result. The discrete delta function can be thought of as a sinc function sampled at all its zeros. Such sampling occurs when the two signals are an integer number of sample points apart.

can be seen in Figure 2, which shows an example similar to Figure 1, but with more complicated incident and reflected fields.

The process becomes further complicated when we attempt to compute the fields at the reflector positions (i.e., at depth) because we normally end up back-propagating reflected energy past the location where it was generated. As the incident field interacts with each successive reflector it produces a series of reflections. Hence, if we only consider the reflected field, energy will suddenly "appear" as each reflector is reached by the incident field. So, once a part of the measured reflected field has been back-propagated into the background model to the location at which it was "added" to the up-going field, it should, in principle, be removed from the reflected field before that field is back-propagated further. However, since back-propagation of the field and the imaging are usually done in separate steps, this removal of energy is not normally done, nor is it likely to be feasible in realistic cases. Thus, nonphysical energy is synthetically back-propagated past the reflector that generated it. This nonphysical energy can "arrive" at a location at the same time as the incident energy, even though there is no reflector at the location where this occurs, leading to artifacts in the image.

A related problem exists for the forward-propagated incident field. In reality, the energy in the incident field is reduced at each reflector, because it is converted into the reflected field. Again, though, this reduction of the incident field at reflector locations is usually not taken into account when forward-propagating the incident field. Additionally, if there are multiple sources of incident (again, usually down-going) energy, it is possible for reflected energy caused by one of the sources to arrive at the same time as the incident energy from another source, potentially causing the appearance of a reflector where there is none.

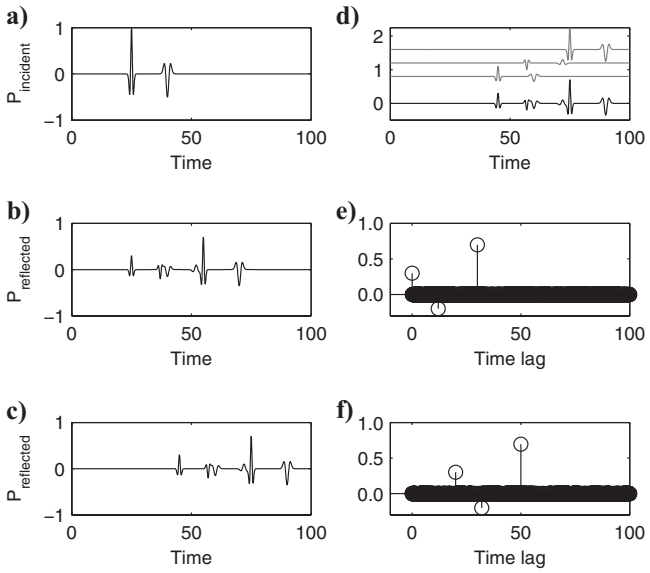

Figure 2. A more complicated example than shown in Figure 1. Again, (a) shows an incident field, now containing two pulses. (b and c) Two possible reflected fields. Both of these reflected fields are shifted versions of that shown in (d), which shows three scaled and shifted versions of the incident field summed to create a single reflected field (the three components are shown in lighter lines, shifted upward for clarity, and the sum is shown in the darker line). (e and f) The result of deconvolution of the two reflected fields to their left. Though the deconvolution is not a single delta function anymore, energy occurs in the zero lag only when a scaled version of the incident field arrives at the same time as the incident field.

These problems with the incident and reflected fields are examples of so-called "crosstalk" and cause significant problems for both deconvolution and crosscorrelation imaging conditions. Put concisely, crosstalk occurs at locations in the image where reflected energy arrives at the same time as incident energy that did not cause the reflected energy. This can occur when some of the energy is nonphysical (and thus only "arrives" at the image point because we have not removed it from the field at the point of reflection), or when fields from two (or more) different sources interact.

In simple cases, deconvolution imaging conditions, which will be formally introduced in the next section, are able to overcome this crosstalk, as will be shown in the examples section. In more complicated cases, this property is not attained, and the complicating factors that cause this to be so are examined in the discussion section. Understanding the cross-talk reducing capabilities of deconvolution imaging conditions, and the limits thereof, becomes more important as these imaging conditions become more commonly used. It is especially important when more complicated down-going fields are used, such as when down-going multiples are treated as secondary ensonification (Muijs et al., 2007a), or if multiple sources fire simultaneously (e.g., Hampson et al., 2008).

DECONVOLUTION IMAGING CONDITIONS

The 1D deconvolution imaging condition is based on equation 1 (Claerbout, 1971):

$$I'_{1D}(x,y,z) = \frac{1}{2\pi}\int_{\omega}\frac{U(x,y,z,\omega)}{D(x,y,z,\omega)}d\omega, \tag{1}$$

where x is the in-line spatial coordinate, y is the cross-line spatial coordinate, z is depth (positive downward), ω is the angular frequency, U is the reflected field (denoted as such because it is usually the upgoing field), and D is the incident field ("D" for down-going). Deconvolution in the time domain is equivalent to division in the frequency domain, hence the quotient U/D. Integrating over frequency gives the zero-time-lag value that would be obtained if we transformed back to the time domain. This can be seen in equation 2 by examining the definition of the inverse Fourier transform given by

$$h(t) = FT^{-1}[H(\omega)] = \frac{1}{2\pi}\int_{-\infty}^{\infty}H(\omega)e^{-i\omega t}d\omega. \tag{2}$$

The corresponding forward Fourier transform in equation 3 is given by

$$H(\omega) = FT[h(t)] = \int_{-\infty}^{\infty}h(t)e^{i\omega t}dt. \tag{3}$$

Equation 1 is not the form of the 1D deconvolution imaging condition that is usually implemented (e.g., Muijs et al., 2007). To avoid division by zero, the top and bottom of the quotient are multiplied by the conjugate of D, which makes the denominator purely real and non-negative. Then, a small real value, ε, can be added to ensure the denominator is not zero. Summation over frequency replaces integration because the data are obtained at a discrete set of frequency values. The resulting image can also be summed over all shots, to give a higher signal to noise ratio as seen in equation 4:

$$I_{1d}(x,y,z) = \frac{1}{2\pi}\sum_{x_{src}} \times\left(\sum_{\omega}\frac{U(x,y,z,\omega;x_{src})D^*(x,y,z,\omega;x_{src})}{D(x,y,z,\omega;x_{src})D^*(x,y,z,\omega;x_{src})+\varepsilon}\Delta\omega\right). \tag{4}$$

Here, x_{src}, is the horizontal position of the source. Note that this is an example of the well-known damped least squares solution (Levenberg, 1944).

The standard crosscorrelation imaging condition is based on this same equation, but goes one step further. The denominator is now purely real and non-negative, so it does not affect the phase of the quotient, and hence it can be approximated by 1 without greatly changing the spatial locations at which zero-lag energy is large (Claerbout, 1971) as seen in equation 5:

$$I_{cross\text{-}cor}(x,y,z) = \frac{1}{2\pi}\sum_{x_{src}}\left(\sum_{\omega}U(x,y,z,\omega;x_{src})D^*(x,y,z,\omega;x_{src})\Delta\omega\right). \tag{5}$$

The 1D deconvolution imaging condition deconvolves two time signals, tacitly assumed to be just scaled and time-shifted versions of one another. This is accurate for a 1D problem, but in cases of 2D or 3D propagation, higher order deconvolution is required. The 2D and 3D deconvolution imaging conditions (Valenciano and Biondi, 2003) corresponding to equation 4 are given by:

$$I_{2D}(x,y,z) = \sum_{k_{xsrc}}\left(\sum_{\omega}\frac{U(x,y,z,\omega;k_{xsrc})D^*(x,y,z,\omega;k_{xsrc})}{D(x,y,z,\omega;k_{xsrc})D^*(x,y,z,\omega;k_{xsrc})+\varepsilon}\frac{\Delta\omega}{2\pi}\right) \times\frac{\Delta k_{xsrc}}{2\pi}, \quad \text{and} \tag{6}$$

$$I_{3D}(x,y,z) = A\sum_{k_{ysrc}}\sum_{k_{xsrc}} \times\left(\sum_{\omega}\frac{U(x,y,z,\omega;k_{xsrc},k_{ysrc})D^*(x,y,z,\omega;k_{xsrc},k_{ysrc})}{D(x,y,z,\omega;k_{xsrc},k_{ysrc})D^*(x,y,z,\omega;k_{xsrc},k_{ysrc})+\varepsilon}\right), \tag{7}$$

where $k_{x\ src}$ is Fourier transform pair of x_{src}, likewise for y_{src} and $k_{y\ src}$, and $A = \Delta\omega\Delta k_{xsrc}\Delta k_{ysrc}/8\pi^3$ in equations 6 and 7. We will examine the motivation for, and benefits of these higher-order deconvolution imaging conditions in the next section.

It should be noted at this point that adding the small term ε to the denominator is not the only way to stabilize the division. Schleicher et al. (2008) examine and compare a number of different methods for stabilizing the denominator, including one introduced by Guitton et al. (2007). As much of our discussion will involve simple analytical situations where we can apply the basic form shown in equation 1, the differences between these various methods will be ignored for the moment. It is sufficient for our purposes to say that various approximations to equation 1 exist, all of which deal with the numerical stability issue, but all of which also introduce some degree of er-

ror. We direct those readers interested in differences between the various methods to Schleicher et al. (2007), in which the types of errors introduced by each method are examined in detail.

In the next section we will examine properties of the deconvolution imaging conditions by looking at simple cases in which analytical solutions can be obtained. Particular attention will be paid to the cross-talk suppressing property of the deconvolution imaging conditions, because this trait would be extremely useful if it could be achieved in realistic situations. Muijs et al. (2007a) touch on this when they make use of the 2D deconvolution imaging condition in their DIPMR methodology, which uses down-going multiple energy as secondary ensonification of the subsurface. Their method eliminates multiples in simple synthetic data sets, but not in the more realistic PLUTO data set, prompting them to develop a multiple-suppression method to accompany the 2D deconvolution imaging condition (Muijs et al., 2007b). Furthermore, if deconvolution imaging conditions could suppress crosstalk in realistic cases, multiple shots could potentially be fired simultaneously without leading to artifacts in the image. This could lead to increased survey efficiency, as the total time required to shoot a desired number of shots could be reduced.

EXAMPLES

To examine the deconvolution imaging conditions and the conditions under which they suppress multiples, we will start with a very simple case and work up to more complicated situations. The simplest case to consider is the 1D imaging condition in equation 1 applied to 1D wave propagation in a medium with constant wave speed, c. The solution to the wave equation in this case is $h(t - z/c)$ for a disturbance propagating in the positive z direction, and $h(t + z/c)$ for a disturbance propagating in the negative z direction, were h is an arbitrary function of t that defines the source pulse shape.

We imagine two pulses travelling in the positive z direction and separated by a time delay, t_0. We can imagine these two pulses as being due to two different sources — due to a single complex source or as a primary and a multiple reflected from some reflector outside our area of consideration; the cause of the second pulse is not important for the illustration, so long as a second pulse is present. Because the wave equation is linear, we can describe the total disturbance as the sum of the two individual disturbances. Thus, the total field traveling in the positive direction can be expressed as seen in equation 8:

$$p_{incident}(z,t) = p_1(t - z/c) + p_2(t - t_0 - z/c). \quad (8)$$

We model a reflector at $z = z_{ref}$, with reflection coefficient R, by including a second pair of reflected disturbances traveling in the negative z direction in equation 9:

$$p_{reflected}(z,t) = Rp_{r1}(z,t) + Rp_{r2}(z,t), \quad (9)$$

where

$$p_{r1}(z,t) = \begin{cases} 0 & t < z_{ref}/c \\ p_1(t + z/c - 2z_{ref}/c & t \geq z_{ref}/c \end{cases}$$
$$p_{r2}(z,t) = \begin{cases} 0 & t < z_{ref}/c + t_0 \\ p_2(t - t_0 + z/c - 2z_{ref}/c & t \geq z_{ref}/c + t_0 \end{cases}. \quad (10)$$

However, because we do not know where the reflector is when we back-propagate the reflected field, we do not know where to apply the zero conditions in equation 10. Thus, the expression that we actually use for the reflected field when applying our imaging condition will be

$$p_{reflected}(z,t) \approx Rp_1(t + z/c - 2z_{ref}/c) + Rp_2(t - t_0 + z/c - 2z_{ref}/c) \quad (11)$$

for all values of t. Note that though z_{ref} appears in the right hand side of equation 11, the data to which we would normally have access would be the left-hand-side, which is a function only of z, and t. In other words, our data would depend on z_{ref} but we would not know its value a priori.

The situation is illustrated in Figures 3 and 4. Figure 3 shows the incident field, as a function of time at a number of different depths. The field at measurement depth, where the field is actually known, is shown at the top of the figure. Each trace below this is a time-shifted version of the measured field, illustrating how we propagate the incident field forward in time as it travels to other depths. Figure 4 shows the reflected field. Again, the top trace is the measured field, and lower traces are time-shifted versions of this. However, in this case, they are shifted backward in time as we propagate the field to depth. We point out that the reflected field is propagated to all depths, despite the fact that it does not really exist for depths deeper than the (as yet unknown) reflector location.

Equations 8 and 11 contain sufficient information to apply the deconvolution imaging condition. First, in equations 12 and 13, we transform the incident and reflected fields to the frequency domain using equation 3:

$$p_{incident}(z,\omega) = e^{-i\omega\frac{z}{c}}P_1(\omega) + e^{-i\omega\left(\frac{z}{c}+t_0\right)}P_2(\omega), \quad (12)$$

and

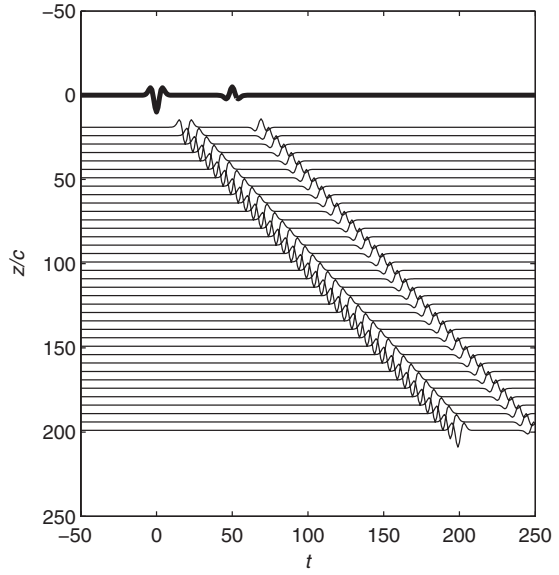

Figure 3. The incident field as a function of time and depth. The top trace represents the measured/known incident field at the receiver depth. All traces below this are the result of propagating the field forward in time to lower depths.

$$p_{reflected}(z,\omega) = e^{i\omega\frac{z-2z_{ref}}{c}}RP_1(\omega) + e^{i\omega\left(\frac{z-2z_{ref}}{c}+t_0\right)}RP_2(\omega), \quad (13)$$

where $P_1(\omega)$ is the Fourier transform of $p_1(t)$, and likewise for P_2. In equation 14, dividing the reflected field by the incident field in the frequency domain is equivalent to deconvolution in the time domain, and gives

$$I_{1d}(z,\omega) = \frac{P_{reflected}(z,\omega)}{P_{incident}(z,\omega)} = Re^{i\omega 2\left(\frac{z-z_{ref}}{c}\right)}. \quad (14)$$

In equation 15, transforming back to the time domain gives

$$I_{1D}(z,t) + = R\delta\left(t - 2\frac{z-z_{ref}}{c}\right). \quad (15)$$

Note that although there were two disturbances involved in the incident and reflected fields, there is only a single delta function in the deconvolution. Hence, if we take the zero-time-lag of this result, we get zero everywhere except at $z = z_{ref}$, which is the location of the reflector. This zero-lag also contains information about the reflection coefficient, R, through simple multiplication.

Contrast this with the result that would be obtained using cross-correlation. Instead of dividing the reflected field by the incident field in the frequency domain, in equation 16 we multiply the conjugate of the incident field by the reflected field, giving

$$\begin{aligned} I_{cross\text{-}cor}(z,\omega) &= P_{reflected}(z,\omega)P^*_{incident}(z,\omega) \\ &= R[P^*_1(\omega)P_1(\omega) + P^*_2(\omega)P_2(\omega)]e^{i\omega\frac{2z-2z_{ref}}{c}} \\ &\quad + R[P^*_1(\omega)P_2(\omega)]e^{i\omega\left(\frac{2z-2z_{ref}}{c}-t_0\right)} \\ &\quad + R[P^*_2(\omega)P_1(\omega)]e^{i\omega\left(\frac{2z-2z_{ref}}{c}+t_0\right)}, \end{aligned} \quad (16)$$

where * indicates the complex conjugate.

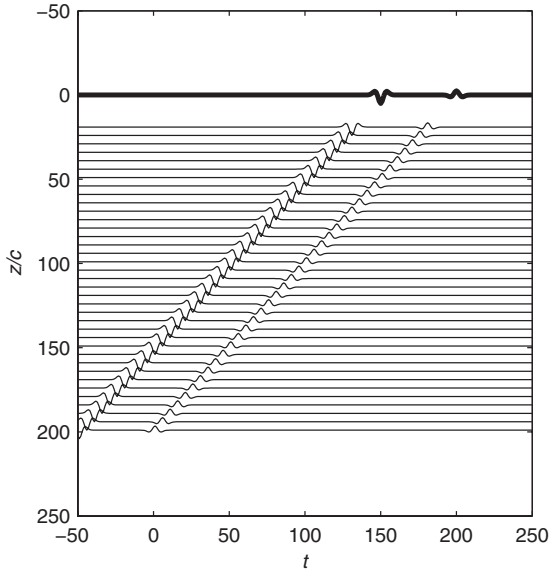

Figure 4. The reflected field as a function of time and depth. The top trace represents the measured/known reflected field at the receiver depth. All traces below this are the result of propagating the field backward in time to lower depths. Compare with the incident field shown in Figure 3.

With crosscorrelation, even if p_1 and p_2 are simple pulses, we obtain three pulses after transformation back to the time domain: the "true" reflection event, but also two other events due to crosstalk between p_1 and p_2. Specifically, there is energy in the zero lag at z $= z_{ref}$ as desired, but also energy in the zero lag at $z = z_{ref} \pm ct_0/2$, which leads to crosstalk in the image, as can be seen in Figure 5, which shows the result of using the two imaging conditions in this case. The deconvolution imaging condition shows one reflector position (75 m), whereas the crosscorrelation imaging condition shows three (50 m, 75 m, 100 m). Also note that the imaged reflectors are wider than that in the deconvolution case, illustrating the superior resolution of the deconvolution imaging condition that we expect after seeing equations 15 and 16.

This simple analytical case shows some advantages of the deconvolution imaging condition: there is improved resolution (because deconvolution provides a delta function, when one function is just a time-shifted and scaled version of the other), and there is a simple relationship between the image magnitude and the reflection coefficient and multiples are eliminated from the image. However, when we move to higher-dimensional propagation, geometric spreading makes imaging more complicated. The 1D deconvolution imaging condition no longer eliminates crosstalk because the signals at two different locations are no longer related through a simple time shift and scaling due to geometric spreading (i.e., a change of receiver position no longer results in just a time shift, but also a change in amplitude as well, and different parts of the signal may be scaled by different amounts). This can be seen by looking at another simple example. Consider a point source in a constant-velocity fluid between two perfectly reflecting surfaces, as shown in Figure 6. The upper surface (at $z = 0$) is a pressure-release surface (like the air-sea boundary), and the lower surface (at $z = h$) is rigid (like an idealized hard sea-

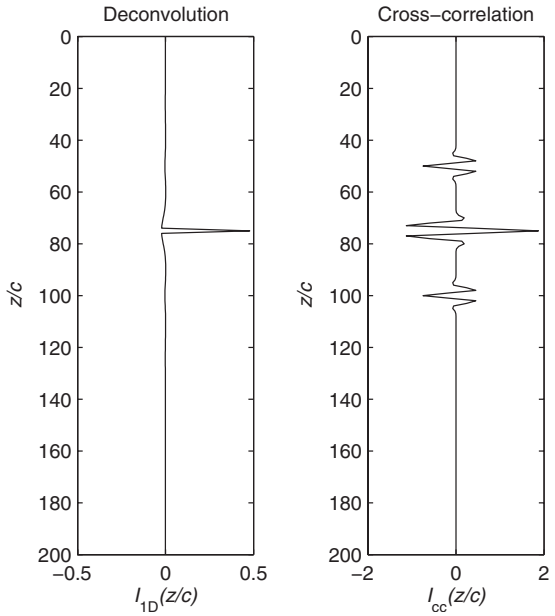

Figure 5. The imaging results for deconvolution (left) and cross-correlation (right) imaging conditions applied to that data in Figures 3 and 4. Deconvolution imaging produces a single, narrow spike, while cross-correlation produces three comparatively broad pulses, even though there was only a single reflector. The extra pulses are due to crosstalk between the different pulses in the incident and reflected fields.

bed). The wavefields can be modelled using the method of images (see, e.g., Frisk, 1994), and for simplicity we consider only the two first down-going waves (from the source and its sea-surface reflection) and the first two up-going waves (the seabed reflection of the two down-going waves). With 3D wave propagation, the down-going field below the source in this case is seen in equations 17–22

$$p_{down}(x,y,z,t) = \frac{1}{r_1}p(t - r_1/c) - \frac{1}{r_2}p(t - r_2/c), \quad (17)$$

where

$$r_1 = \sqrt{(x - x_{source})^2 + (y - y_{source})^2 + (z - z_{source})^2}, \quad \text{and} \quad (18)$$

$$r_2 = \sqrt{(x - x_{source})^2 + (y - y_{source})^2 + (z + z_{source})^2}. \quad (19)$$

The up-going field is

$$p_{up}(x,y,z,t) = \frac{1}{r_3}p(t - r_3/c) - \frac{1}{r_4}p(t - r_4/c), \quad (20)$$

where

$$r_3 = \sqrt{(x - x_{source})^2 + (y - y_{source})^2 + (2h - z_{source} - z)^2} \quad \text{and} \quad (21)$$

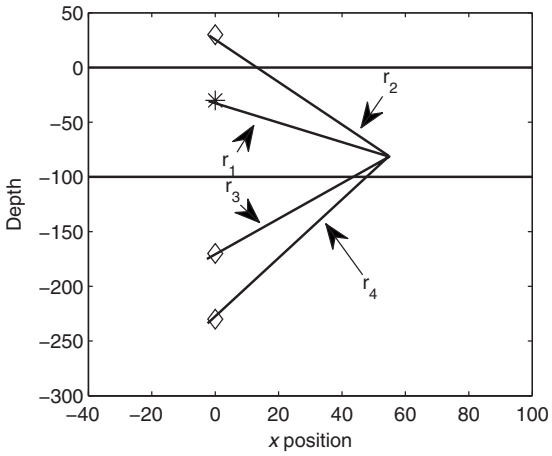

Figure 6. Geometry of a simple case with spreading: a source in an isovelocity medium between two perfect reflectors. The true source is indicated by the asterisk, while the first three image sources are indicated by diamonds. The distances to an arbitrary imaging point are denoted r1 to r4. The horizontal lines indicate positions of the reflectors.

$$r_4 = \sqrt{(x - x_{source})^2 + (y - y_{source})^2 + (2h + z_{source} - z)^2}, \quad (22)$$

and $p(t)$ is the time signature of the source.

At $z = h$, we see that $r_1 = r_3$ and $r_2 = r_4$, and thus $p_{down} = p_{up}$, so the signals deconvolve perfectly to give a single delta function as the result, as we saw in the 1D example. At other depths, however, this is not the case: the r values are not related by a simple multiplicative constant, so the signals do not leave a simple delta function after deconvolution. In particular, where $r_1 = r_4$ or $r_2 = r_3$ there will be significant energy in the zero-lag of the deconvolution, leading to crosstalk in the image, as can be seen in Figure 7.

In such cases, however, higher-dimensional deconvolution imaging conditions can restore some of the multiple-eliminating properties observed in the 1D case. They do so by decomposing the fields into plane waves, and thus avoiding the problems associated with geometric spreading. To do this, the appropriate dimension of deconvolution must be used: 2D deconvolution for 2D spreading problems, and 3D deconvolution for 3D spreading problems. We will first show how the 2D and 3D deconvolution imaging conditions decompose the fields into plane waves, and then examine why doing so eliminates multiples.

The 2D and 3D deconvolution imaging conditions are based on the assumption of a horizontally stratified medium. This assumption makes it possible to decompose the field into plane waves by transforming over the source coordinates rather than x (and y in the 3D case). The advantage of transforming over source position is that the result corresponds to a single location (i.e., image point), whereas transforming over x combines information from all horizontal positions in the subsurface and thus cannot be linked to a single image point.[4] It should be noted that there are other methods of decomposing the wavefield at a single point into plane waves (see Wu et al., 2008, and references within), but they are not directly related to the

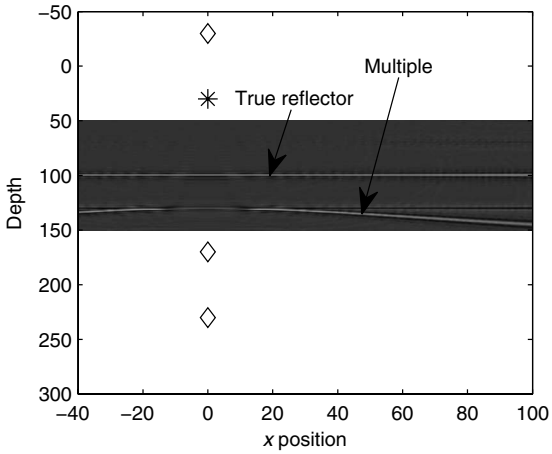

Figure 7. Imaging result using 1D deconvolution with 3D spreading. The true reflector is correctly located, but in this case multiples are not suppressed as they were in the 1D problem.

[4]Of course, if the medium truly were horizontally stratified, we would only need a 1D "image," indicating reflector positions as a function of depth, and the lack of a specific x position in the image would be irrelevant. However, transforming over source position still gives an answer for each x-position, even in cases where our assumption of horizontal stratification is violated, whereas a transformation over x will not. It should be noted that another way of obtaining a plane wave decomposition at a single point would be to take a local transform at each imaging point, using a subset of the data centered at the image point (i.e., a transform from x to k_x using only the data between $x - D$ and $x + D$ for some value D). The added computational load of an extra transform at each image point would be significant; however, in situations where computational limits are not a factor, a local transform over x may well be advantageous.

2D and 3D deconvolution imaging conditions, so we will not discuss them further here.

How is it that we can get the same result when transforming over source position, x_{src}, instead of horizontal position, x? The important thing to realize is that in a horizontally stratified medium, the field depends only on the horizontal distance between the source and the field point, and on the depths of each, but not on the absolute horizontal position of either. Moving the source right while keeping the field point constant will have the same result as moving the field point left while keeping the source's position constant. Thus $p(x,x_{src})$ can be written $p(x - x_{src})$, where dependence on other variables (i.e., y, z, etc.) has been suppressed for clarity. Let us examine the result of transforming such a function over x_{src} and x, and compare the results. First, in equation 23, if we transform over x_{src} we get:

$$\begin{aligned} F_1(k_{xsrc},x) &= FT_{x_{src}\rightarrow k_{xsrc}}[f(x - x_{src})] \\ &= \int_{-\infty}^{\infty} f(x - x_{src}) e^{-ik_{xsrc}x_{src}} dx_{src} \\ &= e^{-ik_{xsrc}x} \int_{-\infty}^{\infty} f(-x') e^{-ik_{xsrc}x'} dx' . \end{aligned} \quad (23)$$

Here we have made use of a change of variable: $x' = x_{src} - x$. Also, we have followed the convention of transforming from x to k_x using a Fourier transform with a sign in the exponent opposite to that used to transform from t to ω. This is done so that a plane wave with a positive wavenumber propagates in the positive x direction as t increases. The 2π factor goes with the transform from k_x to x. See Frisk (1994) for further details on this point.

Next, examine the result of transforming over x in equation 24:

$$\begin{aligned} F_2(k_x,x_{src}) &= FT_{x\rightarrow k_x}[f(x - x_{src})] \\ &= \int_{-\infty}^{\infty} f(x - x_{src}) e^{-ik_x x} dx \\ &= e^{-ik_x x_{src}} \int_{-\infty}^{\infty} f(x'') e^{-ik_x x''} dx'' \end{aligned} \quad (24)$$

Here we have made use of a different change of variable: $x'' = x - x_{src}$. Note that the right-hand sides of equations 23 and 24 are nearly the same. Next, define the function:

$$F_0(k'_x) = \int_{-\infty}^{\infty} f(x') e^{-ik'_x x'} dx' . \quad (25)$$

Note that F_0 is just the Fourier transform of $f(x')f(x')$, and that if the transform of $f(x')$ is $F_0(k_{x'})$, then the transform of $f(-x')$ is $F_0(-k_{x'})$, (Oppenheim, et al., 1997). Combining equations 24 and 25 in equation 26, we see that:

$$F_1(k'_x,x) = e^{-ik'_x x} F_0(-k_x) = e^{-ik'_x(x+x_{src})} F_2(-k'_x,x_{src}). \quad (26)$$

Thus evaluating the transform over x_{src} at k'_x gives the same result as evaluating the transform over x at $-k'_x$ and applying a phase shift that depends on those values of x and x_{src} that were held constant in the two different transforms. Since the transform from x to k_x decomposes the field into plane waves, the transform from x_{src} to $k_{x\ src}$ $R(-k_x)$ does so as well.

Once we have the fields decomposed into their plane-wave components, we can use the fact that the plane wave reflection coefficient is defined as the ratio of the reflected (i.e., up-going) wave to that of the incident (i.e., down-going) wave. If we take the ratios of the two fields at each image point, we get nearly this. Note that the phase shift in equation 26 does not depend on the function being transformed, so it is the same for both fields, and will cancel when they are divided. The quotient will actually be $R(-k_x)$ rather than $R(k_x)$, but because we will sum over all values of k_x when we apply our imaging condition, the result will be the same. The benefit of working in the plane-wave domain is that geometrical spreading is removed from the problem.

Once we have the local reflection coefficient, we can use it to construct the reflected field that would be generated by *any* set of incident plane waves. This can be done by multiplication in the frequency-wavenumber domain as seen in equation 27:

$$P_{reflected}(k_x,f) = R(k_x,f) P_{incident}(k_x,f). \quad (27)$$

This is actually just a restatement of the definition of the reflection coefficient, but it provides an expression for the reflected field for an arbitrary incident field. In particular, we can model the set of down-going plane waves that would be generated by a point source at the image location (i.e., at depth). This is important because it can be related to the image intuitively as follows: using the reflection coefficient, we can construct the reflected wavefield due to that point source. Transforming this reflected field back to the time/space domain gives the reflected component of the impulse response of the imaging location (without the up-going "source" field due to our hypothetical point source at depth) as seen in equation 28:

$$p_{\text{impulse\_response}}(x,t) = FT^{-1}_{k_x\rightarrow x}\{FT^{-1}_{f\rightarrow t}[R(k_x,f)P(k_x,f)]\}. \quad (28)$$

Taking the zero-lag (in both space and time) of the impulse response gives the field that is reflected exactly at the imaging location (non-zero time lags correspond to energy reflected or scattered from other locations that then travels back to the image point, and non-zero space lags corresponds to energy arriving at locations other than the imaging point). If there is no reflector present at the imaging point, then there will be no energy in the zero-lag of the impulse response (again, an impulse response constructed in this way does not contain any up-going energy due to our hypothetical source), and thus no multiples in the image.

Summing the quotient of the up- and down-going fields over frequency and wavenumber is *nearly* the same as taking the zero-lag of the impulse response of the image point. To reconstruct the impulse response of the image point analytically, we must multiply the reflection coefficient by the down-going field generated by an impulsive point source decomposed into plane waves, then transform the result back to the time/space domain. By just summing over frequency and wavenumber without first weighting by the plane wave decomposition of a point source, we obtain an approximation to the zero-lag of the impulse response. The plane wave decomposition of the field due to a point source is $i/k_z e^{ik_z|z-z_{src}|}$ (or just i/k_z at $z = z_{src}$), where $k_z = \sqrt{k^2 - k_x^2}$ in the 2D case, and $k_z = \sqrt{k^2 - k_x^2 - k_y^2}$ in the 3D case, and k is the local wavenumber (see, e.g., Frisk, 1994 for a deri-

vation of this). Not including the i/k_z factor means we do not reproduce a true impulse response of the image point. Instead, the result obtained can be interpreted as the field reflected when unit-amplitude plane waves are simultaneously incident from all directions at once (including imaginary directions, i.e., the evanescent field). This is a somewhat nonphysical, but mathematically acceptable value to use for the image point. Importantly, the field due to this sum of plane waves is impulsive at the imaging point (i.e., all energy arrives at $t = 0$), even though it does not correspond to the field due to an omnidirectional point source. In our experience including the i/k_z factor introduces instability problems (because k_z is zero when the horizontal wavenumber equals the local wavenumber, i.e., horizontal propagation); thus, in most cases including it leads to more errors than does simply ignoring it.

An alternative interpretation of the output of the imaging condition can make the neglect of the i/k_z factor more intuitive. Rather than thinking of the output of the imaging condition as the zero-lag of the impulse response for the image point, we can instead think of it as the angle-averaged value of the reflection coefficient for that point. In such a view, the sum over horizontal wavenumbers does not correspond to a transform back to the space domain for zero spatial offset, but rather just the summing required for taking an average. Thus the i/k_z factor is not required (though a division by the number of horizontal wavenumbers used in the sum would be). An angle-averaged reflection coefficient is less physically meaningful than the zero lag of an impulse response, but it is a sufficiently intuitive quantity that we should not be too uncomfortable in making use of it to form an image. That said, ignoring the i/k_z factor means that we do not obtain a true impulse response of the imaging location, and if the full impulse response is desired rather than just the zero-lag, the factor should be included. However, it should be noted that including or ignoring the i/k_z factor should not have an effect on multiples (since the reflection coefficient does not contain multiples), but it can affect the amplitude of the image and its relation to the true reflector strength.

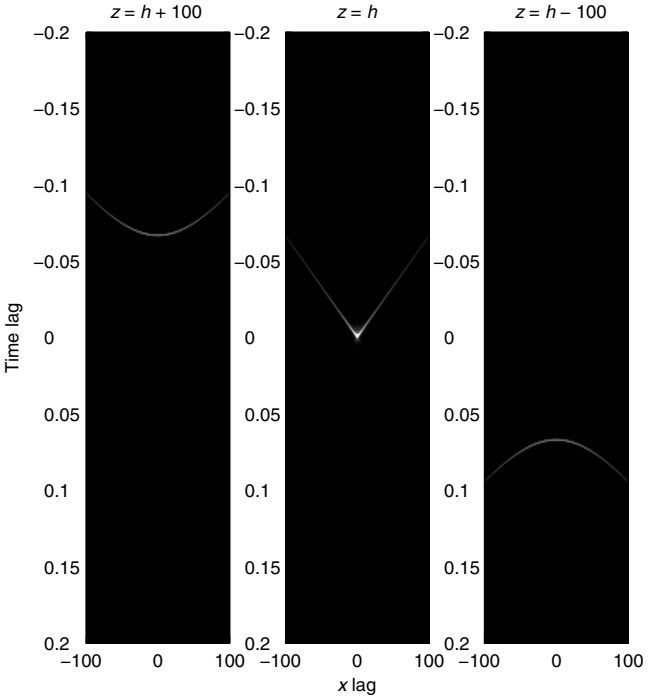

Figure 8. A comparison of the impulse response for a single reflector viewed at three depths. The left panel shows the impulse response at a point below the reflector. At such locations, the up-going, nonphysical, reflected field will arrive before the down-going incident field, and thus energy in the impulse response arrives before $t = 0$. In the middle panel, the depth is the same as the reflector. There is significant energy at the zero time lag. The right panel represents the result for an image point above the reflector. In this case, the down-going energy arrives before the up-going reflected energy, so the impulse response shows energy coming in at positive times. Note that of the three cases, only the $z = h$ case has significant energy at the zero time lag.

This idea of reconstructing the impulse response can be demonstrated analytically, again making use of the relatively simple case of a point source in an constant-velocity layer between two perfectly reflecting interfaces, as shown in Figure 6. We again make use of the method of images, and use only the first two down-going pulses and the first two up-going pulses (i.e., the reflection of the two down-going pulses). In equations 29 and 30, the two fields, in the frequency-wavenumber domain, between $z = z_{source}$ and $z = 2h\text{-}z_{source}$ will be

$$p_{down}(k_x,k_y,z,f) = \frac{i}{k_z}e^{ik_z|z-z_{source}|} - \frac{i}{k_z}e^{ik_z|z+z_{source}|}, \text{ and} \quad (29)$$

$$p_{up}(k_x,k_y,z,f) = \frac{i}{k_z}e^{ik_z|z-(2h-z_{source})|} - \frac{i}{k_z}e^{ik_z|z-(2h+z_{source})|} \quad (30)$$

(see Frisk, 1994). In equation 31, the reflection coefficient is given by the ratio of the reflected (i.e., up-going) field to the incident (i.e., down-going), and the deconvolution imaging condition also uses the quotient of the fields:

$$\frac{p_{up}}{p_{down}} = \frac{e^{ik_z(z-z_{source})} - e^{ik_z(z+z_{source})}}{e^{ik_z(2h-z_{source}-z)} - e^{ik_z(2h+z_{source}-z)}} = \frac{e^{ik_z z}(e^{-ik_z z_{source}} - e^{ik_z z_{source}})}{e^{ik_z(2h-z)}(e^{-ik_z z_{source}} - e^{ik_z z_{source}})} = e^{-ik_z(2h-2z)}. \quad (31)$$

Note that the right-hand side is the plane-wave reflection coefficient for a rigid reflector at depth h: a phase shift equal to twice the vertical distance to the reflector. At the reflector depth, h, the reflection coefficient is 1. If we multiply this reflection coefficient by the plane wave decomposition of a point source at the imaging depth, i/k_z, and transform back to the time/space domain, we get the impulse response of the image point. Examples of this, for three different values of z are shown in Figure 8. Note that when $z = z_{source}$ there is significant energy in the zero-lag, although at the other values of z shown, there is not. Also note that although there were two pulses in the up- and down-going fields, there is only a single arrival in the impulse responses, showing that in this case multiples have been eliminated.

DISCUSSION: WHY DO WE STILL SEE CROSSTALK IN THE IMAGE?

We see analytically that the higher-order deconvolution imaging conditions should eliminate multiples from the image when applied to stratified media of the appropriate dimension of propagation (i.e., 2D deconvolution imaging in the 2D propagation case, and 3D de-

convolution imaging condition in the 3D propagation case). However, a number of numerical issues and other practical limitations will usually keep this analytical result from being obtained, even if the real subsurface were as simple as those described above.

The numerical issues to note are the stabilizing factor, ε, used to avoid division by zero, and the finite values of t and x_{src} to which we are limited in any practical case. The stabilizing factor (or other stabilizing techniques, such as those examined by Schleicher et al., 2008) means that we obtain only an approximate deconvolution of the two fields. This small difference can lead to imperfect elimination of crosstalk at locations where up-going multiple energy arrives at the same time as the down-going direct waves, similar to what is seen when the 1D deconvolution imaging condition was applied to 2D or 3D propagation cases. We can begin to see why this would cause problems by looking at a Taylor expansion of the fraction in equation 4 in terms of ε:

$$\frac{UD^*}{DD^*+\varepsilon} \approx \frac{UD^*}{DD^*} - \varepsilon\frac{UD^*}{(DD^*)^2} + \varepsilon^2\frac{UD^*}{(DD^*)^3} + \ldots \quad (32)$$

We have suppressed the dependencies of U and D in equation 32, as our focus is on ε. The first term in equation 32 is the true, unstabilized value we seek. The higher order terms involve additional deconvolutions of the desired term by DD^*. When transformed back to the time domain, they may well have sufficient energy in the zero-lag to be visible in the image, even when weighted by ε. In fact, with multiples it is less their magnitude that is the problem, and more their coherency in the image.

Another important numerical issue is the finite range of values of t and x_{src} available. When part of one (or both) of the signals "falls off the edge" of our measurement, they will no longer be simply shifted versions of one another. This leads to imperfect deconvolution, as the "missing" portion of the signal is effectively subtracted from the result. For example, in the 2D propagation case, the Green's function for a point source is not time-limited (i.e., it contains energy at all times greater than the first arrival), so any finite time depiction of this signal will actually be missing some of the signal. This is illustrated in Figure 9, which shows imperfect deconvolution in the 2D Green's function case, due to a finite time window. This is not a problem for signals of finite duration, so long as all the energy remains within the time window. However, both the 2D and 3D cases are affected by the finite number of shot and receiver positions, because energy will almost always propagate beyond the bounds of the receiver and source arrays. This is particularly true in the 3D case, where shot locations in the y direction may be limited. Roughly speaking, the energy in the multiples due to this effect will be proportional to the energy that has "fallen off the edge" of our finite measurement. Again, however, the total energy in the multiples is not necessarily the best way to consider their impact, as even low-amplitude multiples stand out in an image due to their coherency.

In addition to these numerical problems, many real-world issues also reduce the multiple-suppressive property of the deconvolution imaging conditions. Most importantly, when a reflection coefficient is not sufficient to represent the up-going field, the result is no longer a true impulse response of the image point. In cases of nonplanar or nonhorizontal layering, an incident-wave at one horizontal wavenumber need not produce only a reflected wave at the same horizontal wavenumber; thus, the reflection coefficient is not a sufficient representation of the reflected field. In such cases, transforming back to the time/space domain does not give the true impulse response of the image point, and there may be nonphysical energy in the zero-lag of the result. In addition, when the subsurface is not horizontally stratified, transforming over source position no longer gives a result equivalent to transforming over field position. This is because the absolute positions of the source and field point matter, not just the difference between the positions, which makes the change of variables used in equations 21 and 22 impossible. Hence, in cases where the subsurface is not perfectly stratified, we should not expect 2D or 3D deconvolution to eliminate multiples, even if numerical issues were not a problem. Other factors, such as attenuation, measurement errors, errors made when propagating the fields into the subsurface, etc., also make it more difficult to obtain the multiple-suppressing property seen in the analytical case, as was observed by Muijs et al., 2007b.

Another important practical consideration is the possibility that the source wavelet is not known. Throughout this article, we have treated the incident field as known/measured, but in many seismic experiments the direct wave is not measured, and a modeled version of it is used as the incident field. This will have an impact on the resolution of the deconvolution imaging conditions, as the reflected field will not be a time-shifted version of the incident field, and the degree to which this degrades the image will depend on how far off the modeled field is from the truth. If the deconvolution of the modeled source pulse from a single reflected pulse is suitably well-behaved, then theoretically the only effect of using the wrong source signature (provided all arrival times are still correct) would be to convolve the image with the function that converts the true source pulse to the modeled pulse. Symbolically,

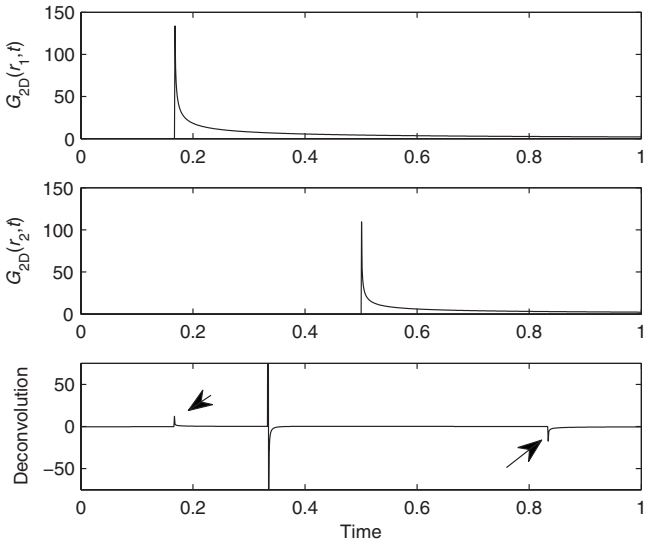

Figure 9. An example of the finite time window resulting in imperfect deconvolution in the case of 2D wave propagation. The top two panels show the 2D isovelocity Green's function as a function of time for two different ranges from the source. The bottom panel shows the result of deconvolving the two signals shown (i.e., using only the times shown in the figures). While the vast majority of energy is concentrated at the correct time-lag (i.e., the difference in the arrival times), the finite time window leads to spurious energy at other times, as indicated by the arrows.

$$D_{\text{Model}}(f) = D_{\text{true}}(f)K(f)$$
$$\Rightarrow \frac{U(f)D^*_{\text{Model}}(f)}{D_{\text{Model}}(f)D^*_{\text{Model}}(f)} = \frac{U(f)D^*_{\text{true}}(f)K^*(f)}{D_{\text{true}}(f)K(f)D^*_{\text{true}}(f)K^*(f)}$$
$$\Rightarrow \frac{U(f)D^*_{\text{Model}}(f)}{D_{\text{Model}}(f)D^*_{\text{Model}}(f)} = \frac{U(f)D^*_{\text{true}}(f)}{D_{\text{true}}(f)D^*_{\text{true}}(f)}\frac{1}{K(f)}. \quad (33)$$

In equation 33, the effect on the image is deconvolution by $K(f)$, which is the function that relates the true source signature with the modeled source signature. Thus, provided a well-behaved $1/K(f)$ exists, the mismatch shouldn't affect the multiple-suppressing ability of the imaging condition. Satisfying the first equation in 33 with a well-behaved $K(f)$, may be nontrivial, however.

Another possibility is that the fields themselves are not known accurately at depth. This can be caused by a number of factors, such as an imperfectly-estimated velocity profile, anisotropy, approximations used in the propagation method, measurement noise, and the fact that nonphysical energy is not removed from the fields at reflector positions when propagating the fields. In principle, we can quantify the errors in our image due to errors in the fields by including error terms in equation 6:

$$D_{\text{Model}}(f) = D(f) + \Delta D(f)U_{\text{Model}}(f) + U(f) + \Delta U(f)$$
$$\Rightarrow \frac{U_{\text{Model}}(f)D^*_{\text{Model}}(f)}{D_{\text{Model}}(f)D^*_{\text{Model}}(f)}$$
$$= \frac{U(f)D^*(f) + \Delta U(f)D^*(f) + U(f)\Delta D^*(f) + \Delta U(f)\Delta D^*(f)}{D(f)D^*(f) + D(f)\Delta D^*(f) + D^*(f)\Delta D(f) + \Delta D(f)\Delta D^*(f)}$$
$$\approx \frac{U(f)D^*(f)}{D(f)D^*(f)} + \frac{\Delta U(f)D^*(f) + U(f)\Delta D^*(f)}{D(f)D^*(f)}$$
$$- \frac{[U(f)D^*(f)][D(f)\Delta D^*(f) + D^*(f)\Delta D(f)]}{[D(f)D^*(f)]^2}. \quad (34)$$

Not knowing what the error terms are, it will not be practical to implement equation 34 directly, but if bounds can be placed on the uncertainties, then a bound on the error in the image could be estimated.

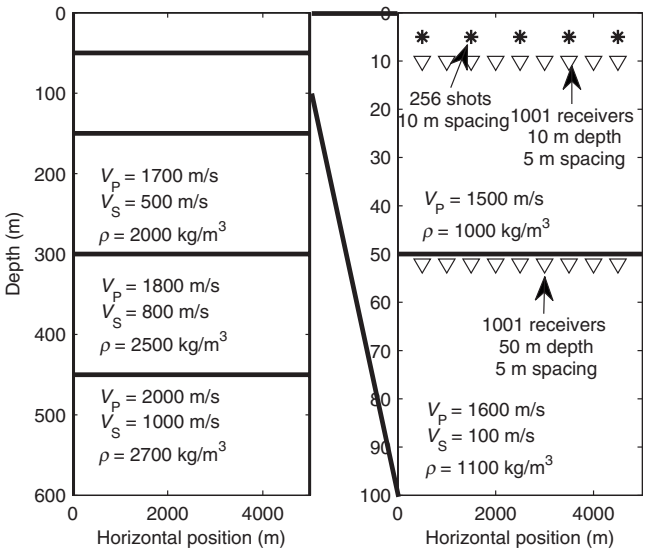

Figure 10. Diagram indicating the parameters used in the synthetic data example, with a zoom-in on the water layer, showing source and receiver configuration.

It should be pointed out that all of these practical issues are mutually confounded, making it almost impossible to study their respective effects in isolation. In any realistic case, a stabilizing approximation will be required to avoid division by zero, and data will be provided only over a finite range of times and positions. Outside of simple analytical cases, these effects will always appear in combination. If the source wavelet is not known, and the subsurface is not horizontally stratified, it will only become more difficult to isolate their individual effects.

An example of practical issues inhibiting the cross-talk suppressing properties is illustrated in Figures 10 and 11. Figure 10 shows the geometry for a simple synthetic data example, with 2D propagation in a horizontally stratified medium. The up- and down-going fields (including the direct wave from the source) were computed for the two geometries shown (one with receivers in the water column, one with receivers just below the water/bottom interface) using the program kxmod from the DELPHI software package produced by the Delphi Consortium. The program models fields for 2D, horizontally layered media, doing the necessary calculations in the frequency-wavenumber domain. Surface-related multiples are computed and included in both fields, and the output is the up- and down-going fields at the receiver positions (thus freeing us from having to decompose the fields into up- and down-going components, and avoiding any numerical errors we might introduce while doing so). Thus, our starting data consisted of four sets, each consisting of 256 $\times$ 1001 traces: An up-going data set for the water-column receivers, a down-going data set for the water-column receivers, an up-going data set for the seafloor receivers, and a down-going data set for the seafloor receivers. Each of the four data sets contained 256 shot gath-

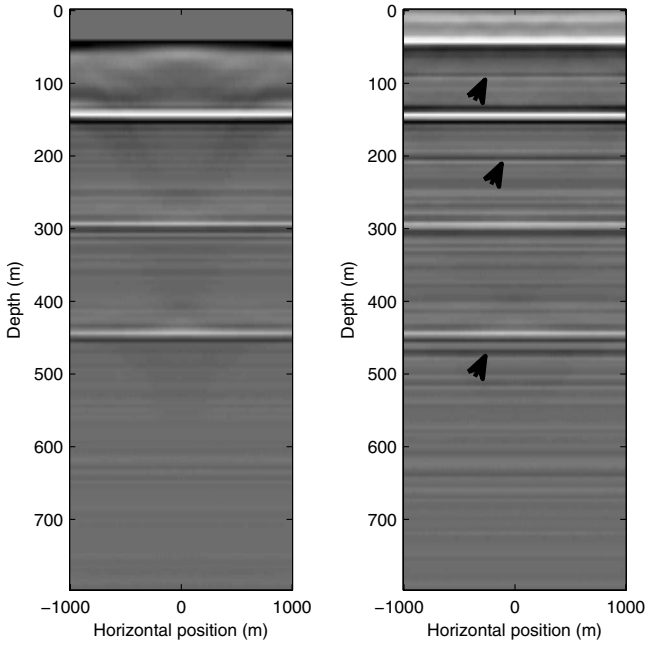

Figure 11. 2D deconvolution imaging result using the data generated in the synthetic experiment depicted in Figure 10. The left panel shows the result when the wavefields are measured just below the seafloor. The right panel shows the result when the wavefields are measured in the water column (where multiple energy is much stronger). Arrows indicate multiple energy in the image that we would not expect to see based on an analytical consideration of the problem with infinite source and receiver ranges.

ers, with each shot gather containing 1001 traces. The distance between the receivers was 5 m, and the distance between source locations was 10 m. We used one-way wave equation methods to downward continue the fields into the subsurface, and applied the 2D deconvolution imaging condition of equation 6 at each image location.

This is a case in which the 2D deconvolution imagine condition should eliminate all multiples (in the analytical case), but as can be seen in Figure 11, multiples still remain in the image. Multiples are particularly strong when the wave fields are measured in the water column (where there is significant multiple energy reflected upward from the seafloor), whereas when the fields are measured just below the seafloor, crosstalk is much less visible in the image. That crosstalk appears in the image is due to the finite range of source and receiver positions, and the stabilizing factor, as described above. The reason multiples are less apparent in the seabed case is that the seafloor and sea surface are the strongest reflectors in the problem, and significant energy is trapped between these two reflectors. When the field is measured just below the seafloor (seabed cables can measure above or just below the seabed, see Muijs et al., 2004), energy that is reflected upward from the seafloor is not included in the up-going field, thus eliminating the major source of multiples in the image.

Figure 12 illustrates some of the effects of the finite source and receiver apertures for the water column measurement case. The top frame shows the magnitude of the multiple around 200 m depth as a function of horizontal position (normalized by the maximum value at this depth), while the bottom shows magnitude of the reflector at 150 m depth (again normalized by the maximum value at this depth). Note that the amplitude of the multiple is stronger away from the center of the image, and the magnitude of the reflector is more constant across horizontal positions. The reduction in amplitude in both plots for positions beyond ~750 m is due to tapering of the fields near the boundaries to reduce edge effects. The model used to generate the data has no dependence on horizontal position, and the same stabilizing constant was used at all spatial positions, so any changes in the image with respect to horizontal position must be due to the effect of the finite apertures. That multiples get stronger nearer to the boundaries (until tapering effects dominant) supports the idea that finite apertures contribute to the problem of incomplete multiple suppression; away from the middle of the image, the numerical case becomes a poorer approximation to the analytical (i.e., infinite aperture) case.

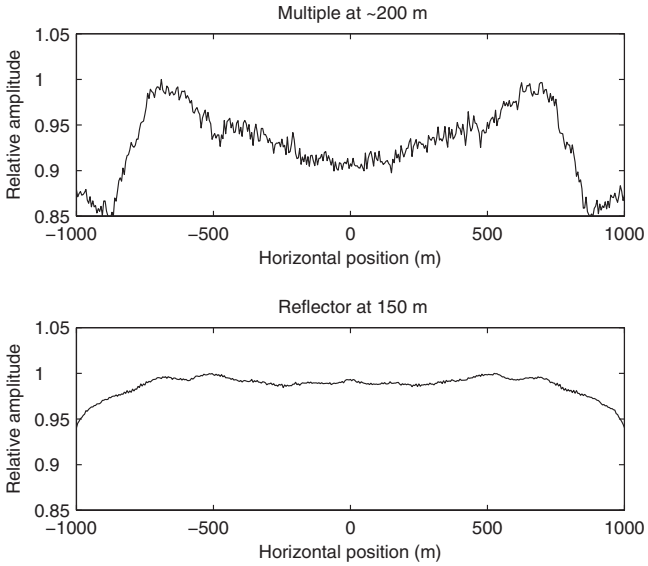

Figure 12. Magnitudes as a function of horizontal position for a multiple (top) and reflector (bottom). The top frame shows the magnitude of the multiple in the image at ~200 m depth, normalized to the maximum value at that depth. The bottom frame shows the magnitude of the reflector in the image at 150 m depth. The reduction of both at offsets greater than 750 m from the center of the figure is due to tapering of the fields to avoid edge effects. Note that the magnitude of the multiple increases away from the center of the image, supporting the idea that finite aperture effects can lead to increased multiple energy.

There are, of course, options for addressing some of the issues described in this section. The most obvious is to apply existing multiple elimination methods to the data as is done for crosscorrelation-based imaging. There is extensive literature on surface-related multiple elimination and we will not attempt to cover it here. Suffice to say, though, that there is nothing to prevent us from applying the same methods normally used with crosscorrelation imaging when we instead use deconvolution imaging. If we do so, we will still benefit from the higher resolution and closer to true amplitude properties of deconvolution.

An option for reducing the effects of nonphysical energy in the fields used to compute the image is to use the full two-way wave equation. Doing so will not entirely eliminate nonphysical energy, because we do not know the locations of reflectors until we have created the image. However, the additional accuracy in the estimated fields should translate into an improved image. Another option is to incorporate the imaging result into the subsurface model and perform a second migration of the data, now with approximate knowledge of reflector positions and strengths. This is very similar to the method suggested by Muijs et al. (2007b). Using a two-way wave equation-based migration method (such as reverse time migration) in such a case would likely lead to an improvement in the image.

Another option would be to make use of the fact that most of the multiple energy is due to reflections at the seafloor. Unlike the other reflectors, the seafloor's location should be well-known before we have created the image. Modeling water column peg legs may be feasible, and would allow one to adaptively subtract multiple energy from the fields before imaging. This would be similar to existing demultiple methods, such as Verschuur et al. (1992), but might include explicit modeling based on knowledge of the bathymetry.

CONCLUSIONS

Deconvolution imaging conditions offer a number of useful properties compared to standard crosscorrelation imaging conditions. Deconvolution imaging conditions offer superior resolution, reflector amplitudes more directly related to reflection coefficients, and multiple-suppression in some simple analytic cases. It is also worth noting that the 2D and 3D deconvolution imaging conditions offer a way to compute an estimate of the full impulse response of a given subsurface location, though this is not typically done.

The multiple suppression capability of deconvolution imaging conditions is limited due to a number of practical issues, including stabilization requirements, signals extending past finite measurement apertures, and a requirement of horizontal stratification. Thus, they should not be counted on to deliver multiple free images. However, this fact should not preclude the use of deconvolution imaging conditions; the improved resolution and amplitudes alone justify their use.

ACKNOWLEDGMENTS

The authors thank the Delphi research consortium for the use of the DELPHI software, which was used to generate the synthetic data used to generate Figure 10. We also thank Simon King, Thomas Guest, Phil Kitchenside, Susanne Rentsch, Massimiliano Vassallo, and the reviewers for their helpful comments and suggestions that improved the manuscript. We also thank WesternGeco for funding provided for this research.

REFERENCES

Claerbout, J. F., 1971, Toward a unified theory of reflector mapping: Geophysics, **36**, 467–481, doi: 10.1190/1.1440185.

Frisk, G. V., 1994, Ocean and seabed acoustics: a theory of wave propagation: Prentice-Hall, Inc.

Guitton, A., A. Valenciano, D. Bevc, and J. Claerbout, 2007, Smoothing imaging condition for shot profile migration: Geophysics, **72**, no. 3, S149–S154, doi: 10.1190/1.2712113.

Hampson, G., J. Stefani, and F. Herkenhoff, 2008, Acquisition using simultaneous sources: The Leading Edge, **27**, 918–923, doi: 10.1190/1.2954034.

Levenburg, K., 1944, A method for the solution of certain non-linear problems in least squares: Quarterly of Applied Mathematics, **2**, 164–168.

Muijs, R., J. O. A. Robertsson, and K. Holliger, 2004, Data-driven adaptive decomposition of multicomponent seabed recordings: Geophysics, **69**, 1329–1337, doi: 10.1190/1.1801949.

———, 2007a, Prestack depth migration of primary and surface-related multiple reflections: Part I — Imaging: Geophysics, **72**, no. 2, S59–S69, doi: 10.1190/1.2422796.

———, 2007b, Prestack depth migration of primary and surface-related multiple reflections: Part II — Identification and removal of residual multiples: Geophysics, **72**, no. 2, S71–S76, doi: 10.1190/1.2424544.

Oppenheim, A. V., A. S. Wilsky, and S. H. Nawab, 1997, Signals and systems, 2nd Edition: Prentice Hall, Inc.

Schleicher, J., J. C. Costa, and A. Novais, 2008, A comparison of imaging conditions for wave-equation shot profile migration: Geophysics, **73**, no. 6, S219–S227, doi: 10.1190/1.2976776.

Valenciano, A., and B. Biondi, 2003, 2D deconvolution imaging condition for shot profile migration: 73rd Annual International Meeting, SEG, Expanded Abstracts, 1059–1062.

Verschuur, D. J., A. J. Berkhout, and C. P. A. Wapenaar, 1992, Adaptive surface-related multiple elimination: Geophysics, **57**, 1166–1177, doi: 10.1190/1.1443330.

Wu, R., Y. Wang, and M. Luo, 2008, Beamlet migration using local cosine basis: Geophysics, **73**, no. 5, S207–S217, doi: 10.1190/1.2969776.